Experimental and Thermodynamic Assessment of the Nb-Ni-Y System

N. Mattern, M. Zinkevich, W. Löser, G. Behr, and J. Acker

(Submitted February 20, 2007; in revised form October 15, 2007)

Phase equilibria in the ternary Nb-Ni-Y system are studied experimentally for the first time using x-ray diffraction, electron probe microanalysis, and differential scanning calorimetry in combination with levitation experiments. No ternary compounds exist, while the solubility of third element in binary solid phases is negligible. A subsolidus isothermal section at 750 °C, fields of primary crystallization, invariant reactions, as well as an extension of the liquid miscibility gap from the Nb-Y binary system are determined. Thermodynamic model description for the Nb-Ni-Y system including the binary Nb-Y subsystem is developed and used for calculations of the projection of liquidus surface, isothermal, and vertical sections.

1. Introduction

Phase separation in bulk metallic glasses has now attracted considerable interest because the introduction of suitable inhomogeneities is an important concept to improve the mechanical properties, especially to increase the ductility.[1] The amorphous structure formation in these novel metallic materials is achieved by rapid quenching of the melt; however, they exhibit nanoscale composition inhomogeneities, which are "frozen in" into a two-phase amorphous alloy. This interesting behavior has already been demonstrated for a five-component Zr-Y-Ni-Cu-Al alloy[2] and a quaternary Co-Al-Ni-Y alloy.[3] Only recently have phase separated metallic glasses of a ternary system Nb-Ni-Y been prepared by rapid quenching from the melt.[4]

Generally, alloys for new phase-separated metallic glasses are designed by combining elements with high glass-forming ability with an element having strong tendency to demix at least for one of the other main constituents. The rapid solidification of such alloys leads to special hierarchical microstructures. The understanding of microstructure formation is rather poor and requires the knowledge of the thermodynamic data of the alloy systems, which are practically unknown until now. So far, the ternary Nb-Ni-Y system is the simplest system of this type and

offers the unique possibility for thermodynamic calculations as a basis for understanding the formation of phase-separated metallic glasses. Therefore, in this paper the Nb-Ni-Y phase diagram is experimentally as well as thermodynamically assessed. The CALPHAD method[5] is best suited for this purpose, since it allows easy calculation of unknown phase equilibria in multicomponent systems based on the Gibbs energies of constituent phases in the lower-order binary and ternary systems, in terms of known thermodynamic and phase equilibria data.

2. Sample Preparation and Methods of Investigation

Ingots of the alloys were melted from 99.9 wt.% Nb and 99.99 wt.% Ni and Y (Alfa Aesar) in an argon arc furnace, using a nonconsumable tungsten electrode on a water-cooled copper hearth. The alloys were remelted four times; the ingot was inverted after each melt to promote mixing. The mass of each ingot was about 30 g. The ingots were wrapped in tantalum foil, annealed at 750 to 1000 °C for 24 h in sealed silica ampoules under 15 kPa purified Ar gas and then quenched into water. Specimens of a selected composition (about 2 g) were heated in a levitation apparatus under high-purity argon atmosphere to temperatures above the liquidus. Temperature was measured by a pyrometer. By switching off the levitation field, the melt became rapidly quenched on a copper plate.

Three exact weights per samples close to 50 mg were dissolved in 5 mL concentrated hydrochloric acid (Merck, p.a.) at 180 °C for 15 min by microwave digestion (μPrep, MWS) using 100 mL Teflon vessels. The diluted sample solutions were prepared by weighing and were adjusted to a total hydrochloric acid concentration of 5 wt.%. Chemical analysis was performed by inductively coupled plasma optical emission spectrometry (ICP-OES) by a radial IRIS Intrepid II XUV (Thermo Corp., Franklin, MA) with an Echelle optics, a charge injection device (CID) detector for

N. Mattern, W. Löser, and **G. Behr**, Leibniz-Institut für Festkörper- und Werkstoffforschung IFW Dresden, Helmholtzstraße 20, D-01069 Dresden, Germany; **M. Zinkevich**, Max Planck Institut für Metallforschung, Heisenbergstraße 3, D-70569 Stuttgart, Germany; **J. Acker**, Leibniz-Institut für Festkörper- und Werkstoffforschung IFW Dresden, Helmholtzstraße 20, D-01069 Dresden, Germany; and **J. Acker**, Fachhochschule Lausitz, Großenhainer Straße 57, D-01968 Senftenberg, Germany. Contact e-mail: N.Mattern@ifw-dresden.de.

simultaneous recording of the selected emission lines, and a cyclonic glass spray chamber with SeaSpray nebulizer. The analytical results are obtained from the background corrected emission intensities of at least three different emission lines of each element. All measurements were performed in the so-called bracketing mode by placing a sample between two standards to compensate for time-dependent drift effects. Each sample was measured in three different runs to improve the statistical significance. This procedure yields typical uncertainties in the element contents of 0.5 % RSD (1 σ) and below.

X-ray diffraction analysis (XRD) was conducted with a Panalytical XPERT'Pro Bragg-Brentano diffractometer (PANALYTICAL, Almelo, The Netherlands) using Co Kα radiation and a diffracted beam graphite monochromator. Powders with a particle size of ≤ 100 μm were prepared from ingots using a hard metal mortar and pestle as well as a sieve. X-ray diffraction patterns $I(2\theta)$ were recorded for 2θ values from 20.0° to 120° with a step size of 0.05°, and a measuring time of 5 s per step. For qualitative and quantitative phase analysis, the whole pattern Rietveld method was applied.

All samples were prepared for metallographic examination by polishing the resin-mounted specimens with diamond pastes. The microstructure was analyzed by scanning electron microscopy (SEM) in the backscattered electron (BSE) imaging mode using a Philips XL30 (PHILIPS, Eindhoven, The Netherlands). The chemical composition of the individual phases was measured by electron probe x-ray microanalysis (EPMA) using wavelength-dispersive x-ray (WDX) spectroscopy for determination of solubilities as well as energy-dispersive (EDX) for chemical phase characterization. Binary Ni-Nb and Ni-Y alloys were used as standard materials. The characteristic wavelengths of Nb Lα, Ni Kα, and Y Lα were detected to determine the concentration of the elements using an acceleration voltage of 20 kV. The area of the analyzing window on the specimen surface was between 1 by 1 μm and 50 by 50 μm, depending on the microstructure. The standard deviations of the element concentration were calculated from three to five independent measurements, moving the electron probe each time to a new position.

Differential scanning calorimetry (DSC) studies of the annealed samples were done using a Netzsch DSC 404 (NETZSCH, Selb, Germany) at a heating rate of 20 K/min up to 1400 to 1500 °C in an argon atmosphere.

3. Thermodynamic Modeling

The Gibbs energy of each element is defined with respect to its stable magnetically disordered state at 298.15 K and 10^5 Pa (stable element reference). In the SGTE-Pure database,[6] the Gibbs energy is represented as a power series in terms of temperature in the form:

$$°G(T) = a + bT + cT\ln(T) + dT^2 + eT^3 + f/T + \sum_n g_n T^n$$

(Eq 1)

where a to f and g_n are coefficients and n represents a set of integers. The reference states for the pure niobium, nickel,

Table 1 Summary of thermodynamic parameters describing the Nb-Ni-Y system referred to the stable element reference H^{SER} (T = 298.15 K, P = 100 kPa). Values are given in SI units (J, mol, and K), except β (μ$_B$ per mole of atoms)

Parameter	Ref
$G_{Nb}^{bcc}, G_{Nb}^{fcc}, G_{Nb}^{cph}, G_{Nb}^{liq}, G_{Ni}^{bcc}, G_{Ni}^{fcc}, G_{Ni}^{cph}, G_{Ni}^{liq}, G_{Y}^{bcc}, G_{Y}^{fcc}, G_{Y}^{hcp}, G_{Y}^{liq}$	6
$^0L_{Nb,Ni}^{liq} = -96,160 + 22T$	8
$^1L_{Nb,Ni}^{liq} = 104,000 - 45T$	8
$^0L_{Ni,Y}^{liq} = -15,5496 + 38.932T$	8
$^1L_{Ni,Y}^{liq} = -52,904 + 6.785T$	8
$^0L_{Nb,Y}^{liq} = +188,000 - 61.3T$	This work
$^1L_{Nb,Y}^{liq} = +39,500$	This work
$^0L_{Nb,Ni,Y}^{liq} = +33,700$	This work
$^1L_{Nb,Ni,Y}^{liq} = -22,800$	This work
$^2L_{Nb,Ni,Y}^{liq} = +184,350$	This work
$^0L_{Nb,Ni}^{fcc} = -110,300 + 39.5T$	8
$^1L_{Nb,Ni}^{fcc} = +40,000$	8
$^0L_{Ni,Y}^{fcc} = -2,000$	15
$^0L_{Nb,Y}^{fcc} = +100,000$	This work
$(T_C)_{Ni}^{fcc} = 633; \beta_{Ni}^{fcc} = 0.52$	6
$^0(T_C)_{Nb,Ni}^{fcc} = -2,500; {}^0\beta_{Nb,Ni}^{fcc} = 0$	8
$^0L_{Nb,Ni}^{bcc} = -28,000 + 20T$	8
$^0L_{Ni,Y}^{bcc} = -2,000$	15
$^0L_{Nb,Y}^{bcc} = +150,000$	This work
$(T_C)_{Ni}^{bcc} = 575; \beta_{Ni}^{bcc} = 0.85$	6
$^0L_{Nb,Ni}^{cph} = +150,000$	This work
$^0L_{Ni,Y}^{cph} = -2,000$	15
$^0L_{Nb,Y}^{cph} = +150,000$	This work
$G_{Nb:Ni}^{NbNi_8} = -145,000 + 46T + G_{Nb}^{bcc} + 8G_{Ni}^{fcc}$	8
$G_{Nb:Ni}^{NbNi_3} = -128,100 + 33T + G_{Nb}^{bcc} + 3G_{Ni}^{fcc}$	8
$G_{Ni:Nb}^{NbNi_3} = +168,100 - 33T + 3G_{Nb}^{bcc} + G_{Ni}^{fcc}$	8
$G_{Nb:Nb}^{NbNi_3} = +20,000 + 4G_{Nb}^{bcc}$	8
$G_{Ni:Ni}^{NbNi_3} = +20,000 + 4G_{Ni}^{fcc}$	8
$G_{*:Nb,Ni}^{NbNi_3} = +100,000$	8
$G_{Nb,Ni:*}^{NbNi_3} = 0$	8
$G_{Nb:Nb:Nb:Ni:Ni}^{\mu} = -279,000 + 58T + 7G_{Nb}^{bcc} + 6G_{Ni}^{fcc}$	8
$G_{Ni:Nb:Nb:Nb:Ni}^{\mu} = -285,000 + 58T + 6G_{Nb}^{bcc} + 7G_{Ni}^{fcc}$	8
$G_{Ni:Nb:Nb:Ni:Ni}^{\mu} = -296,000 + 58T + 4G_{Nb}^{bcc} + 9G_{Ni}^{fcc}$	8
$G_{Nb:Nb:Nb:Nb:Nb}^{\mu} = +130,000 + 13G_{Nb}^{bcc}$	8
$G_{Ni:Nb:Nb:Nb:Nb}^{\mu} = +130,000 + 12G_{Nb}^{bcc} + G_{Ni}^{fcc}$	8
$G_{Nb:Nb:Nb:Ni:Nb}^{\mu} = +130,000 + 11G_{Nb}^{bcc} + 2G_{Ni}^{fcc}$	8
$G_{Ni:Nb:Nb:Ni:Nb}^{\mu} = +130,000 + 10G_{Nb}^{bcc} + 3G_{Ni}^{fcc}$	8
$G_{Nb:Nb:Nb:Ni:Ni}^{\mu} = -290,000 + 58T + 5G_{Nb}^{bcc} + 8G_{Ni}^{fcc}$	8
$G^{Ni_{17}Y_2} = -379,600 + 57.635T + 17G_{Ni}^{fcc} + 2G_{Y}^{cph}$	This work
$G^{Ni_5Y} = -186,706 + 31.187T + 5G_{Ni}^{fcc} + G_{Y}^{cph}$	15
$G^{Ni_4Y} = -160,555 + 22.979T + 4G_{Ni}^{fcc} + G_{Y}^{cph}$	15
$G^{Ni_7Y_2} = -294,966 + 38.770T + 7G_{Ni}^{fcc} + 2G_{Y}^{cph}$	15
$G^{Ni_3Y} = -134,358 + 16.477T + 3G_{Ni}^{fcc} + G_{Y}^{cph}$	15
$G^{Ni_2Y} = -101,736 + 8.988T + 2G_{Ni}^{fcc} + G_{Y}^{cph}$	15
$G^{NiY} = -67,151.8 + 5.5642T + G_{Ni}^{fcc} + G_{Y}^{cph}$	15
$G^{Ni_2Y_3} = -162,837.5 + 32.5369T + 2G_{Ni}^{fcc} + 3G_{Y}^{cph}$	15
$G^{NiY_3} = -84,446 + 14.1911T + G_{Ni}^{fcc} + 3G_{Y}^{cph}$	15

and yttrium are: body-centered cubic (bcc) Nb, a hypothetical magnetically disordered face-centered cubic (fcc) Ni, and close-packed hexagonal (cph) Y, respectively. The

corresponding coefficients for stable and metastable structures are taken from the compilation of Dinsdale.[6] Equation 1 also applies for the stoichiometric compounds and end members of solutions. The ordered intermetallic phases with a homogeneity range are represented by sublattice models based on compound energy formalism[7] as follows:[8] $(Nb,Ni)(Nb)_2(Nb)_2(Nb,Ni)_2(Nb,Ni)_6$ for the μ-phase, and $(Nb,Ni)(Nb,Ni)_3$ for the NbNi$_3$-phase.

The liquid and disordered solid solutions, bcc, fcc, and cph are described using a substitutional solution model, the Gibbs energy being defined as:

$$G^\phi = \sum_{i=1}^{3} x_i G_i^{ref} + G^{id} + G^{ex}; \quad G^{id} = RT\sum_{i=1}^{3} x_i \ln(x_i)$$

$$G^{ex} = \sum_{i=1}^{3}\sum_{j>i}^{3} x_i x_j \sum_{v=0}^{n} {}^v L_{i,j}(x_i - x_j)^v + x_i x_j x_k {}^0 L_{i,j,k}$$

(Eq 2)

where G_i^{ref} is the reference Gibbs energy of the pure element i, that is, Nb, Ni, or Y in the corresponding form φ; G^{id} is the ideal mixing contribution; G^{ex} is the excess energy; x_i, x_j, and x_k are the mole fractions of the constituents i, j, and k, respectively. ${}^v L_{i,j}$ is the binary interaction parameter of
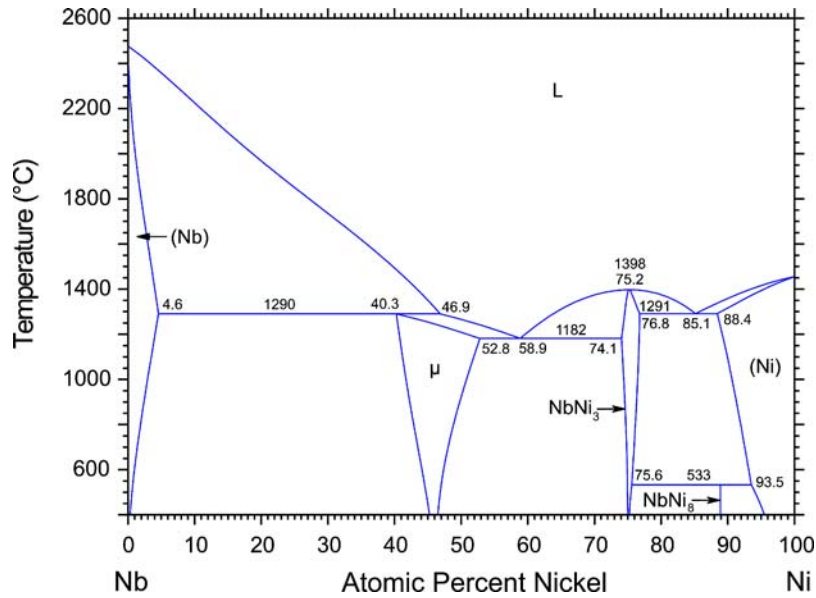

Fig. 1 Nb-Ni phase diagram calculated using the thermodynamic description from Ref 8
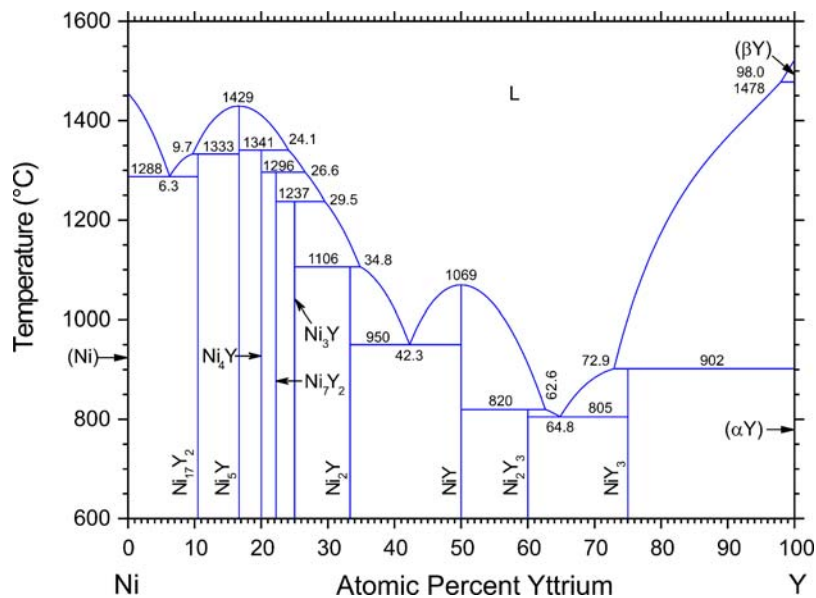

Fig. 2 Calculated Ni-Y phase diagram based on thermodynamic assessment from Ref 15

components i and j of an order ν, and $L_{i,j,k}$ is the ternary interaction parameter. The latter has the following composition dependence:

$$L_{\mathrm{Nb,Ni,Y}} = x_{\mathrm{Nb}}{}^{0}L_{\mathrm{Nb,Ni,Y}} + x_{\mathrm{Ni}}{}^{1}L_{\mathrm{Nb,Ni,Y}} + x_{\mathrm{Y}}{}^{2}L_{\mathrm{Nb,Ni,Y}} \qquad \text{(Eq 3)}$$

Magnetic contributions into the Gibbs energy of fcc and bcc phases are taken into account according to the treatment proposed by Hillert and Jarl.[9]

The thermodynamic model parameters for the ternary system Nb-Ni-Y are evaluated on the basis of the experi-
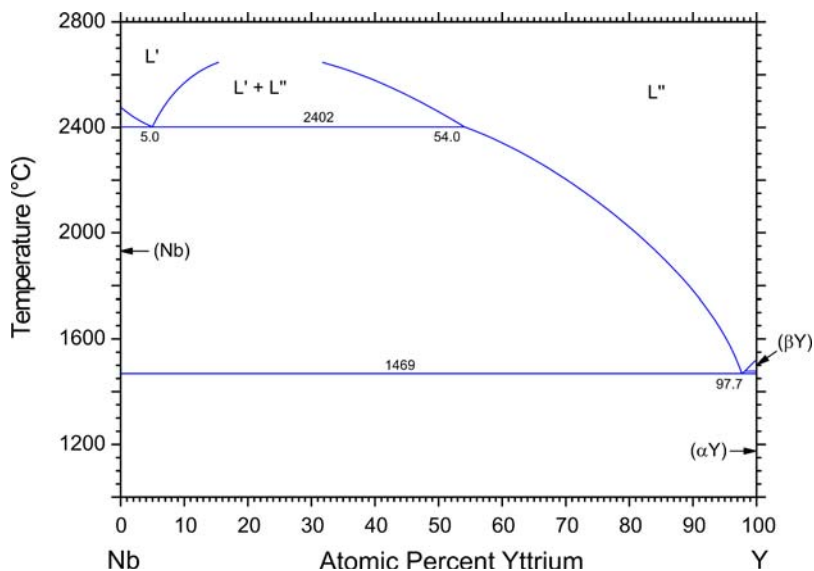
Fig. 3 The Nb-Y phase diagram optimized and calculated in this work
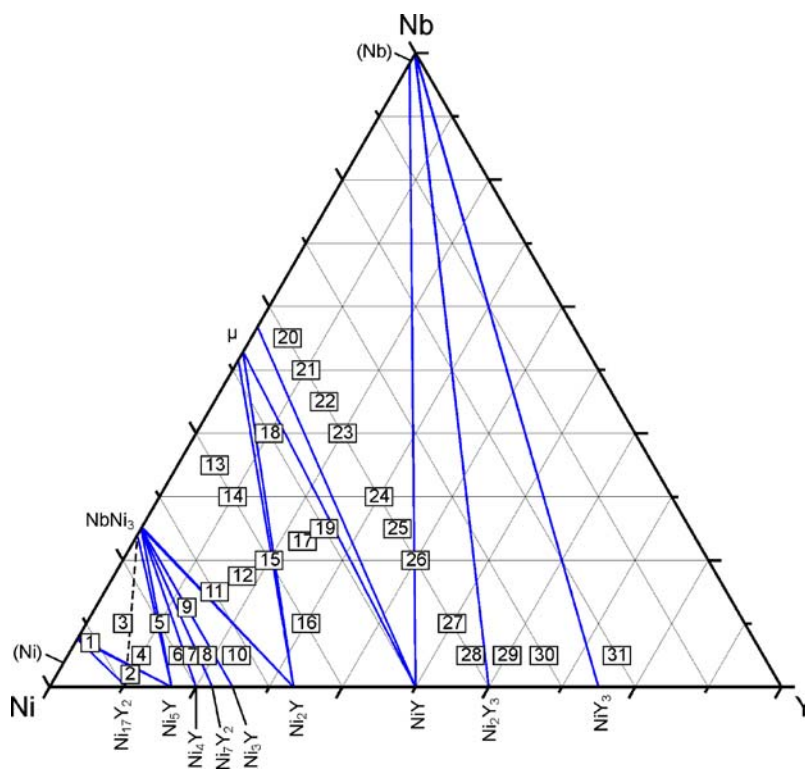
Fig. 4 Calculated isothermal section of the Nb-Ni-Y system at 750 °C in atomic percents. Squared numbers correspond to the investigated alloys (Table 2). Dashed line shows the Ni$_{17}$Y$_2$-NbNi$_3$ equilibrium calculated with the initial thermodynamic parameters of Ni$_{17}$Y$_2$ phase from Ref 15

Table 2 Results of phase analysis of ternary Nb-Ni-Y alloys annealed at 750 °C for 24 h

No.	Composition of alloy, at.%		Phases observed by XRD	Phases observed by SEM/EDX
	Nominal	ICP-OES		
1	$Ni_{91}Nb_7Y_2$	$Ni_{91.00}Nb_{7.03}Y_{1.97}$	$(Ni) + Ni_{17}Y_2$	$(Ni) + Ni_{17}Y_2$
2	$Ni_{88}Nb_2Y_{10}$	$Ni_{88.35}Nb_{2.04}Y_{9.61}$	$(Ni) + Ni_{17}Y_2 + Ni_5Y$	$(Ni) + Ni_5Y$
3	$Ni_{85}Nb_{10}Y_5$	$Ni_{85.16}Nb_{9.92}Y_{4.92}$	$(Ni) + Ni_5Y$	$(Ni) + Ni_5Y + NbNi_3$
4	$Ni_{85}Nb_5Y_{10}$	$Ni_{85.29}Nb_{5.02}Y_{9.68}$	$(Ni) + Ni_5Y + NbNi_3$	$(Ni) + Ni_5Y + NbNi_3$
5	$Ni_{80}Nb_{10}Y_{10}$	$Ni_{80.38}Nb_{9.99}Y_{9.63}$	$Ni_5Y + NbNi_3$	$Ni_5Y + NbNi_3$
6	$Ni_{80}Nb_5Y_{15}$	$Ni_{80.46}Nb_{4.97}Y_{14.57}$	$Ni_5Y + Ni_4Y + NbNi_3$	$Ni_5Y + Ni_4Y + NbNi_3$
7	$Ni_{78}Nb_5Y_{17}$	$Ni_{78.57}Nb_{4.77}Y_{16.66}$	$Ni_5Y + Ni_4Y + NbNi_3(a)$	$Ni_5Y + Ni_4Y + NbNi_3$
8	$Ni_{76}Nb_5Y_{19}$	$Ni_{76.66}Nb_{4.90}Y_{18.44}$	$Ni_3Y + Ni_7Y_2 + NbNi_3$	$Ni_3Y + NbNi_3$
9	$Ni_{75}Nb_{12.5}Y_{12.5}$		$Ni_3Y + NbNi_3$	$Ni_3Y + NbNi_3$
10	$Ni_{72}Nb_5Y_{23}$	$Ni_{72.68}Nb_{5.04}Y_{22.28}$	$Ni_3Y + Ni_2Y + NbNi_3$	$Ni_2Y + NbNi_3$
11	$Ni_{70}Nb_{15}Y_{15}$	$Ni_{71.77}Nb_{13.2}Y_{15.03}$	$Ni_2Y + NbNi_3$	$Ni_2Y + NbNi_3$
12	$Ni_{65}Nb_{17.5}Y_{17.5}$		$Ni_2Y + NbNi_3 + \mu$	
13	$Ni_{60}Nb_{35}Y_5$	$Ni_{60.21}Nb_{34.93}Y_{4.86}$	$Ni_2Y + NbNi_3 + \mu$	$Ni_2Y + NbNi_3 + \mu$
14	$Ni_{60}Nb_{30}Y_{10}$	$Ni_{60.22}Nb_{29.30}Y_{10.47}$	$Ni_2Y + NbNi_3 + \mu$	
15	$Ni_{60}Nb_{20}Y_{20}$	$Ni_{60.80}Nb_{19.59}Y_{19.61}$	$Ni_2Y + \mu$	$Ni_2Y + \mu$
16	$Ni_{60}Nb_{10}Y_{30}$	$Ni_{60.47}Nb_{10.03}Y_{29.50}$	$Ni_2Y + NiY + \mu$	
17	$Ni_{54}Nb_{23}Y_{23}$	$Ni_{54.90}Nb_{25.00}Y_{20.10}$	$Ni_2Y + NiY + NbNi_3$	
18	$Ni_{50}Nb_{40}Y_{10}$	$Ni_{56.5}Nb_{32.63}Y_{10.87}$	$Ni_2Y + \mu$	
19	$Ni_{50}Nb_{25}Y_{25}$	$Ni_{54.74}Nb_{18.72}Y_{26.53}$	$Ni_2Y + NiY + \mu$	
20	$Ni_{40}Nb_{55}Y_5$	$Ni_{40.71}Nb_{54.35}Y_{4.94}$	$\mu + (Nb)$	
21	$Ni_{40}Nb_{50}Y_{10}$	$Ni_{39.46}Nb_{53.12}Y_{7.4}$	$NiY + \mu + (Nb)$	
22	$Ni_{40}Nb_{45}Y_{15}$	$Ni_{40.03}Nb_{46.68}Y_{13.29}$	$NiY + \mu + (Nb)$	
23	$Ni_{40}Nb_{40}Y_{20}$		$NiY + (Nb) + Ni_2Y(a)$	$NiY + \mu + (Nb) + Ni_2Y$
24	$Ni_{40}Nb_{30}Y_{30}$	$Ni_{40.90}Nb_{30.34}Y_{28.76}$	$NiY + \mu + (Nb) + Ni_2Y(a)$	$NiY + \mu + (Nb)$
25	$Ni_{40}Nb_{25}Y_{35}$	$Ni_{41.42}Nb_{19.94}Y_{38.64}$	$NiY + \mu + (Nb)$	
26	$Ni_{40}Nb_{20}Y_{40}$	$Ni_{41.46}Nb_{17.72}Y_{40.82}$	$NiY + (Nb)$	
27	$Ni_{40}Nb_{10}Y_{50}$	$Ni_{41.12}Nb_{9.11}Y_{49.77}$	$NiY + (Nb) + Ni_2Y_3$	$NiY + (Nb) + Ni_2Y_3$
28	$Ni_{40}Nb_5Y_{55}$		$NiY + (Nb) + Ni_2Y_3$	
29	$Ni_{35}Nb_5Y_{60}$		$NiY_3 + (Nb) + Ni_2Y_3$	
30	$Ni_{30}Nb_5Y_{65}$		$NiY_3 + (Nb) + Ni_2Y_3$	
31	$Ni_{20}Nb_5Y_{75}$		$NiY_3 + (Nb) + (Y)$	

(a) The existence of this phase is questionable due to its low amount

Table 3 Solubility of third element in binary phases and homogeneity range of solid solutions in the Nb-Ni-Y system as determined by EPMA after heat treatment for 24 h

Phase	Equilibrium	Heat treatment, °C	Solubility, at.%
$NbNi_3$	$NbNi_3 + \mu + Ni_2Y$, $NbNi_3 + Ni_5Y$	1000	0.05 (Y)
μ	$\mu + Ni_2Y + NbNi_3$	1000	0.18 (Y)
Ni_5Y	$Ni_5Y + Ni_4Y + NbNi_3$	1000	0.2 (Nb)
Ni_3Y	$Ni_3Y + Ni_7Y_2 + NbNi_3$	1000	0.5 (Nb)
Ni_2Y	$Ni_2Y + NbNi_3 + \mu$	800	0.1 (Nb)
NiY	$NiY + Ni_2Y + \mu$	800	<0.02 (Nb)
Ni_2Y_3	$Ni_2Y_3 + NiY + (Nb)$	800	<0.02 (Nb)
(Nb)	$(Nb) + \mu + NiY$	1000	0.1 (Y), 2.0 (Ni)
(Ni)	$(Ni) + Ni_5Y$	1000	8.3 (Nb)

mental information of this work using the least-squares optimization module PARROT of the multicomponent thermodynamic software Thermo-Calc.[10] All phase diagrams are calculated with PANDAT software.[11] The final thermodynamic parameters are given in Table 1.

4. Binary Systems

In the Nb-Ni system, three intermetallic phases, $NbNi_8$ (stable below 535 °C), $NbNi_3$, and Nb_7Ni_6 (μ-phase) are known. Terminal solid solutions fcc (Ni) and bcc (Nb) show significant homogeneity ranges. Several thermodynamic assessments of the Nb-Ni system have been reported in recent years.[8,12,13] In general, the calculated phase diagrams are very similar (in the older work[12] the $NbNi_8$ phase is not present). Differences in the Nb-rich liquidus and in the homogeneity range of the μ-phase are due to the use of different thermodynamic data from literature for the
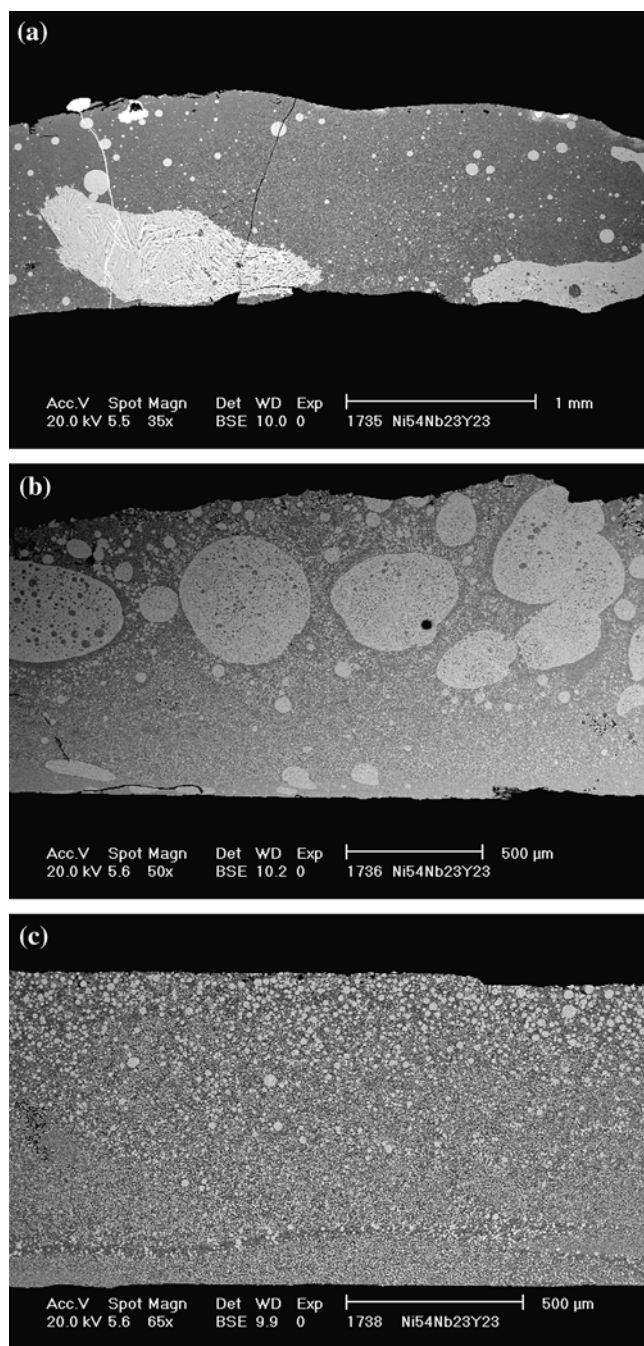
Fig. 5 SEM micrograph of the microstructure of alloy 17 ($Ni_{54.90}Nb_{25.00}Y_{20.10}$) levitated and quenched from temperatures of (a) 1300, (b) 1400, and (c) 1500 °C

Table 4 Chemical compositions of the two immiscible liquids in alloy 17 ($Ni_{54.90}Nb_{25.00}Y_{20.10}$) as determined by EDX after levitation and quenching

Temperature, °C	Composition, at.%	
	Liquid 1	Liquid 2
1200	$Ni_{50}Nb_{45}Y_5$	$Ni_{58}Nb_{11}Y_{31}$
1300	$Ni_{50}Nb_{43}Y_7$	$Ni_{58}Nb_{13}Y_{29}$
1400	$Ni_{50}Nb_{40}Y_{10}$	$Ni_{58}Nb_{17}Y_{25}$
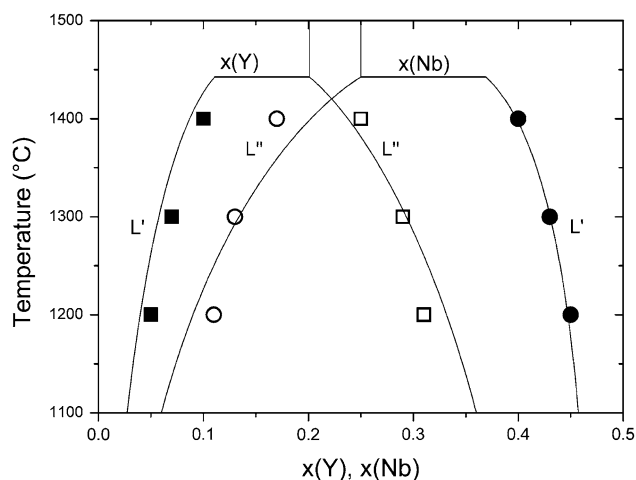
Fig. 6 Calculated Nb and Y contents in two liquids in alloy 17 ($Ni_{54.90}Nb_{25.00}Y_{20.10}$) compared with experimental data (all solid phases were disregarded). Nb measurements are given by squares, Y measurements by circles, solid symbols for L′, and open symbols for L″

optimization. In the present work, the description of Joubert et al.[8] is selected because of the better agreement with experimental tie-lines in the subsolidus region. The calculated Nb-Ni binary phase diagram is shown in Fig. 1.

Nine intermetallic phases exist in the Ni-Y system, that is, $Ni_{17}Y_2$, Ni_5Y, Ni_4Y, Ni_7Y_2, Ni_3Y, Ni_2Y, NiY, Ni_2Y_3, and NiY_3. A thermodynamic assessment of the Ni-Y system is reported by Du and Zhang[14] and was updated very

recently.[15] It is accepted in the present work with a minor adjustment of parameters of $Ni_{17}Y_2$ phase to provide a match between experimental and calculated tie-lines in the Ni-rich part of the ternary Nb-Ni-Y system. This modification results in somewhat different values of the enthalpy and entropy of formation of the $Ni_{17}Y_2$ compound, but not in any changes in calculated phase diagram (Fig. 2). Note that the experimental thermodynamic data for solid phases in the Ni-Y system are missing.

An experimental Nb-Y phase diagram has been reported by Palenzona and Cirafici.[16] No thermodynamic description is available in the literature. The Nb-Y system is characterized by an extensive immiscibility in the liquid and complete immiscibility in the solid state. The critical temperature of the liquid miscibility gap is unknown. The Gibbs energy parameters of phases in the Nb-Y system are estimated in this work based on the limited experimental phase equilibria data[16] and using present results on the extension of the liquid miscibility gap into the ternary Nb-Ni-Y system as an additional constraint. All phases are described as substitutional solutions. The calculated Nb-Y

binary phase diagram is shown in Fig. 3. Using regular and subregular interaction parameters for the liquid phase, it was possible to obtain a good fit of the eutectic and monotectic temperatures, 1470 ± 10 °C and ~2400 °C, respectively.[16] The eutectic composition is calculated at 97.7 at.% Y to compare with the experimental value of 94 ± 0.5 at.%.[16] The agreement can only be improved by using higher-order interaction terms, but the necessary experimental data, especially on liquidus are lacking. The calculated composition of the Y-rich liquid at the monotectic temperature is in good agreement with the value of 54 at.% Y given in the literature. The yttrium content in the Nb-rich liquid is 5.0 at.% according to the present assessment. The experimental value is reported as ~0.5 at.% and thus cannot be considered reliable. The calculated solid solubilities of Y in Nb and vice versa are around 0.1 at.% in agreement with experimental reports,[16] while niobium has virtually no effect on the temperature of polymorphic cph $\leftrightarrow$ bcc transformation in yttrium metal (1478 °C).

5. Ternary System

5.1 Isothermal Section at 750 °C

In order to minimize the experimental efforts, the isothermal section of the Nb-Ni-Y system at 750 °C was first calculated by extrapolation from binary subsystems using Muggianu interpolation of binary excess terms.[17] The interaction parameters ${}^0L_{\mathrm{Nb,Y}}^{\mathrm{fcc}}$ and ${}^0L_{\mathrm{Nb,Ni}}^{\mathrm{cph}}$ were given large positive values to avoid the artificial stabilization of fcc and cph phases in the Nb-Y and Nb-Ni systems, respectively, and in the adjacent regions of the Nb-Ni-Y system. For the NbNi$_3$ and μ-phase, the two and five sublattice models were used as originally proposed by

Joubert et al.,[8] while all other phases, that is, NbNi$_8$,[8] and Ni-Y intermetallics[15] were treated as stoichiometric compounds. The temperature of 750 °C was chosen to ensure that all alloys were completely in the solid state. The calculated isothermal section is shown in Fig. 4.

The nominal compositions of alloys for experimental investigation were chosen to check the different three- and two-phase fields suggested by extrapolating calculation. The results of the quantitative phase analysis by XRD and EPMA are summarized in Tables 2 and 3. The results of chemical analysis show (Table 2) that for most alloys the deviation from nominal composition does not exceed 1 at.%. In general, arc melting resulted in some deficiency of Y because of the higher evaporation rate of this metal compared with Nb and Ni. However, the microstructure of some alloys (see below) revealed compositional inhomogeneities because of the liquid immiscibility or primary crystallization of (Nb), which could not be dissolved during subsequent annealing at 750 °C. In such a case, the chemical analysis gives the composition of only a part of the ingot. Some alloys also showed the presence of four phases due to the incomplete equilibration. Since no ternary compounds and no significant solubility of third element in binary solid phases were observed, the subsolidus phase equilibria in the Nb-Ni-Y system were determined by the relative Gibbs energies of phases in binary subsystems; that is, no ternary interaction parameters for solid solutions were required. A comparison of Table 2 and Fig. 4 reveals that the extrapolating calculation is already in agreement with experiment, except the phase relations in the Ni corner. According to the published thermodynamic description of Ni-Y system,[15] Ni$_{17}$Y$_2$ forms tie-lines with NbNi$_3$ (dashed line in Fig. 4) instead of experimentally confirmed Ni$_{17}$Y$_2$-(Ni) equilibrium. A small modification of the Gibbs energy expression of Ni$_{17}$Y$_2$ phase (see above) removed this inconsistency. In summary, the 750 °C isothermal section of

Table 5 Calculated temperatures (calc) and compositions of phases at the invariant equilibria in the Nb-Ni-Y system compared with experimental data (exp) of this work

| Equilibrium | Temperature, °C | | Calculated | | | | | | | |
	calc	exp	Y, at.%				Nb, at.%			
U$_1$: L + Ni$_{17}$Y$_2$ $\leftrightarrow$ Ni$_5$Y + (Ni)	1247	1256	5.4	10.5	16.7	~0	6.3	nil	nil	7.9
U$_2$: L + Ni$_5$Y $\leftrightarrow$ NbNi$_3$ + Ni$_4$Y	1234	1235	16.4	16.7	nil	20.0	9.4	nil	25.0	nil
U$_3$: L + Ni$_4$Y $\leftrightarrow$ NbNi$_3$ + Ni$_7$Y$_2$	1204	1191	19.3	20.0	nil	22.2	8.4	nil	25.1	nil
U$_4$: L + Ni$_7$Y$_2$ $\leftrightarrow$ NbNi$_3$ + Ni$_3$Y	1162	1161	22.9	22.2	nil	25.0	7.1	nil	25.1	nil
U$_5$: L + Ni$_3$Y $\leftrightarrow$ NbNi$_3$ + Ni$_2$Y	1058	1063	30.7	25.0	nil	33.3	4.0	nil	25.3	nil
U$_6$: L + NbNi$_3$ $\leftrightarrow$ μ + Ni$_2$Y	1026	1035	33.0	nil	nil	33.3	4.2	25.7	48.9	nil
U$_7$: L + (Nb) $\leftrightarrow$ μ + NiY	1021	1008	44.4	~0	nil	50.0	1.2	96.9	58.4	nil
E$_1$: L $\leftrightarrow$ Ni$_5$Y + (Ni) + NbNi$_3$	1227	1224	4.2	16.7	~0	nil	10.2	nil	11.0	23.3
E$_2$: L $\leftrightarrow$ μ + Ni$_2$Y + NiY	936	930	41.0	nil	33.3	50.0	1.1	53.2	nil	nil
M$_1$: L' + L'' + (Nb) $\leftrightarrow$ μ	1262	1304	5.0	31.0	~0	nil	43.8	11.5	95.6	59.6
D$_1$: L + (Nb) + (Y) $\leftrightarrow$ NiY$_3$	902	895	72.9	~0	99.9	75.0	~0	99.9	~0	nil
D$_2$: L + (Nb) $\leftrightarrow$ Ni$_2$Y$_3$ + NiY$_3$	805	802	64.8	~0	60.0	75.0	~0	99.8	nil	nil
D$_3$: L + (Nb) + NiY $\leftrightarrow$ Ni$_2$Y$_3$	820	809	62.6	~0	50.0	60.0	~0	99.8	nil	nil
e$_1$(max): L $\leftrightarrow$ Ni$_5$Y + NbNi$_3$	1291		7.9	16.7	nil	⋯	11.8	nil	24.5	⋯
e$_2$(max): L $\leftrightarrow$ NiY + (Nb)	1059		50.5	50.0	~0	⋯	0.6	nil	98.3	⋯
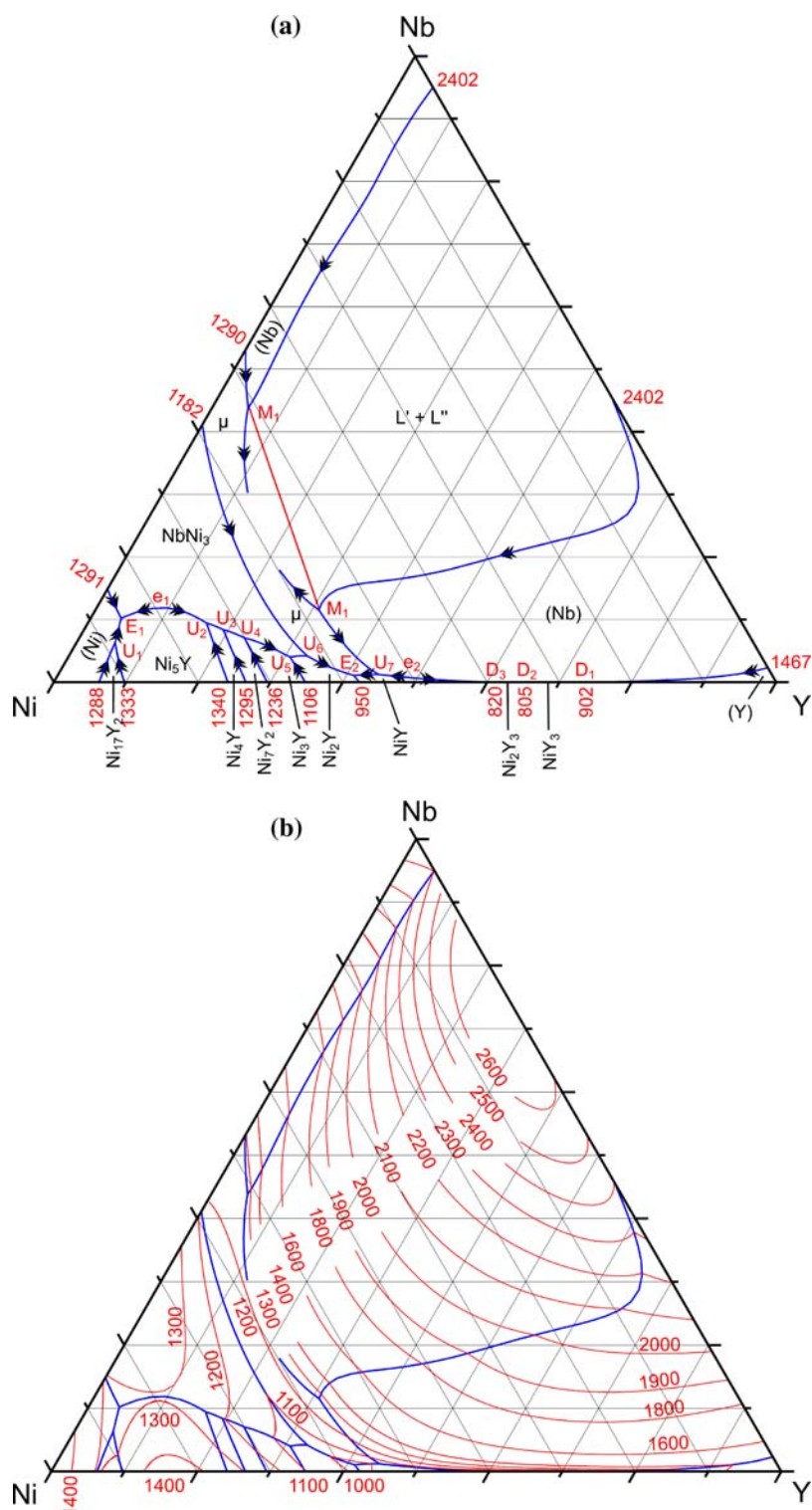
Fig. 7 Calculated projection of liquidus surface in the ternary Nb-Ni-Y system in atomic percents. (a) Monovariant liquidus lines with the indicated fields of primary crystallization and invariant points. (b) Liquidus isotherms in °C

the Nb-Ni-Y system in the Ni-rich part is dominated by the NbNi$_3$ phase, which forms tie-lines with Ni$_5$Y, Ni$_4$Y, Ni$_7$Y$_2$, Ni$_3$Y, and Ni$_2$Y, while beyond 50 at.% Y it consists of equilibria formed by (Nb) with NiY, Ni$_2$Y$_3$, and NiY$_3$. The μ-phase of Nb-Ni system is stable in the intermediate range of compositions and coexists with both Ni$_2$Y and NiY.
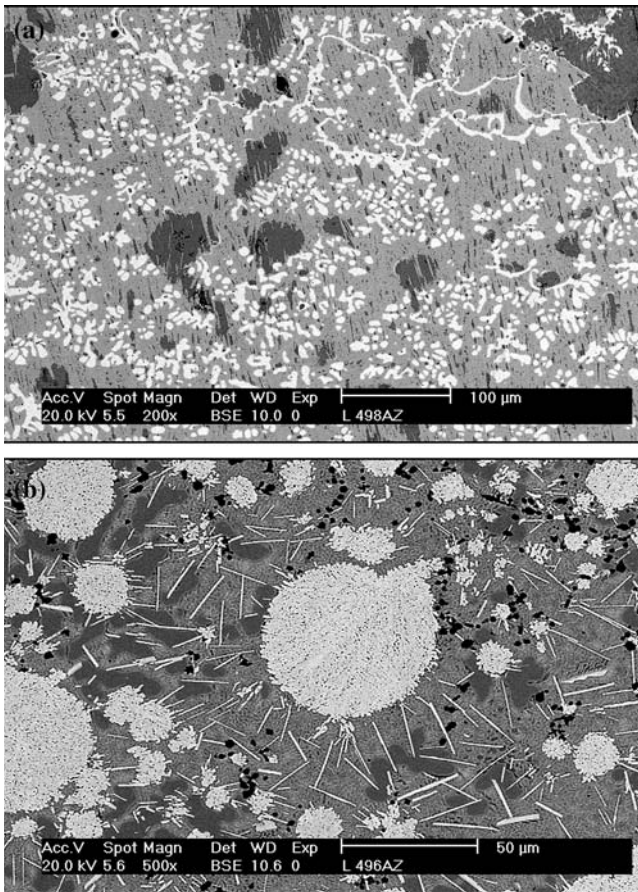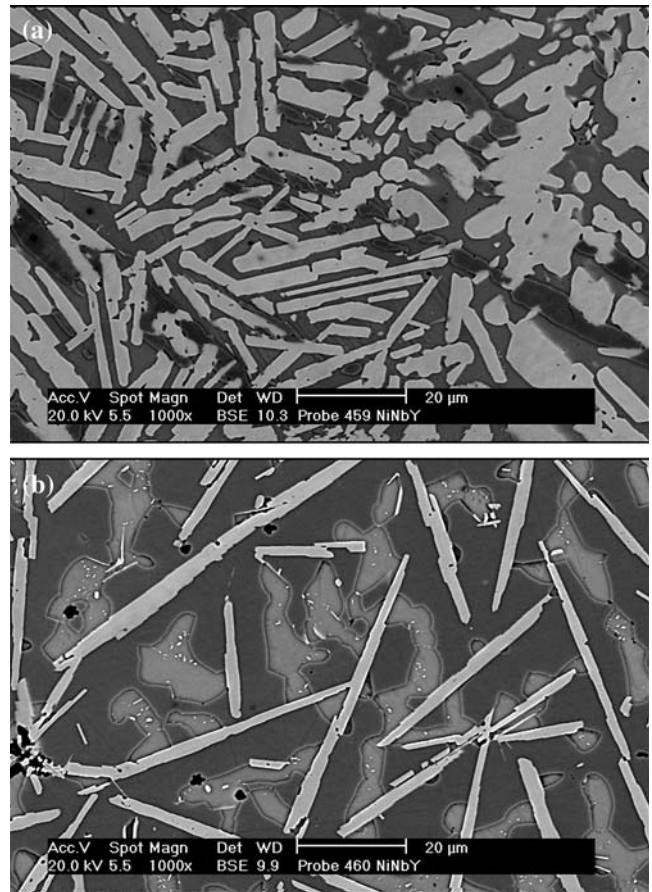
Fig. 8 SEM micrographs of the solidification microstructures of alloys within the liquid immiscibility region. (a) Alloy 23 ($Ni_{40}Nb_{40}Y_{20}$): white, (Nb); gray matrix, μ; dark, NiY. (b) Alloy 19 ($Ni_{54.74}Nb_{18.72}Y_{26.53}$): light spherical particles and needles, μ; dark, Ni_2Y; gray matrix, μ + Ni_2Y + NiY; black spots, pores

Fig. 9 SEM micrographs of the solidification microstructures of alloys in the region of the primary crystallization of the μ-phase. (a) Alloy 14 ($Ni_{60.22}Nb_{29.30}Y_{10.47}$): white, μ; gray matrix, Ni_2Y; dark, $NbNi_3$. (b) Alloy 16 ($Ni_{60.47}Nb_{10.03}Y_{29.50}$): white needles, μ; dark, Ni_2Y; gray, NiY

5.2 Liquid Immiscibility

Extrapolating calculation revealed a quite extensive protrusion of the liquid miscibility gap from the Nb-Y binary into the ternary Nb-Ni-Y system. Indeed, the microstructures of the solidified alloys 17, 19, 23, and 24 suggest that a phase separation into two liquids took place before a primary crystallization occurred. Experimental information on the ternary liquid miscibility gap was obtained by analyzing the microstructure of samples, which had been levitated in the liquid state and quenched. Figure 5 shows SEM micrographs of the microstructure of alloy 17 quenched from three different temperatures, as an example. For $T = 1300$ (Fig. 5a) and 1400 °C (Fig. 5b) large inhomogeneities are visible, Nb-enriched white regions and Y-enriched gray regions. Also some spherical white precipitates confirm that this microstructure is caused by the phase separation in the melt. At the same time, the microstructure of the sample quenched from 1500 °C (Fig. 5c) shows only small particles or spheres of Ni-Nb phases within the Ni-Y matrix. These particles are formed by phase separation of the homogeneous liquid during quenching followed by the crystallization. The critical temperature is evident in the

DSC curve by an endothermic event at $T = 1475$ °C upon heating. The chemical compositions of both the liquid phases in alloy 17 were determined by EDX analysis integrating over large regions of the individual particles. The results (Table 4) indicate that apart from the Nb:Y ratio, the melts are different in Ni content.

The calculated Nb and Y contents in two liquids in alloy 17 are in reasonable agreement with experimental data, as shown in Fig. 6. All solid phases were disregarded in the calculation to allow the metastable extrapolation to low temperatures. The critical temperature of the miscibility gap for this composition was predicted at 1443 °C. It should be noted that the plots shown do not represent a vertical section through the Nb-Ni-Y phase diagram because of different Ni contents in the two liquids.

5.3 Solidification Behavior and Projection of Liquidus Surface

The equilibrium solidification paths of alloys 1 to 11, 14 to 16, 19, 23, 24, and 27 to 31 were reconstructed by analyzing their arc melted, as-cast microstructures. This
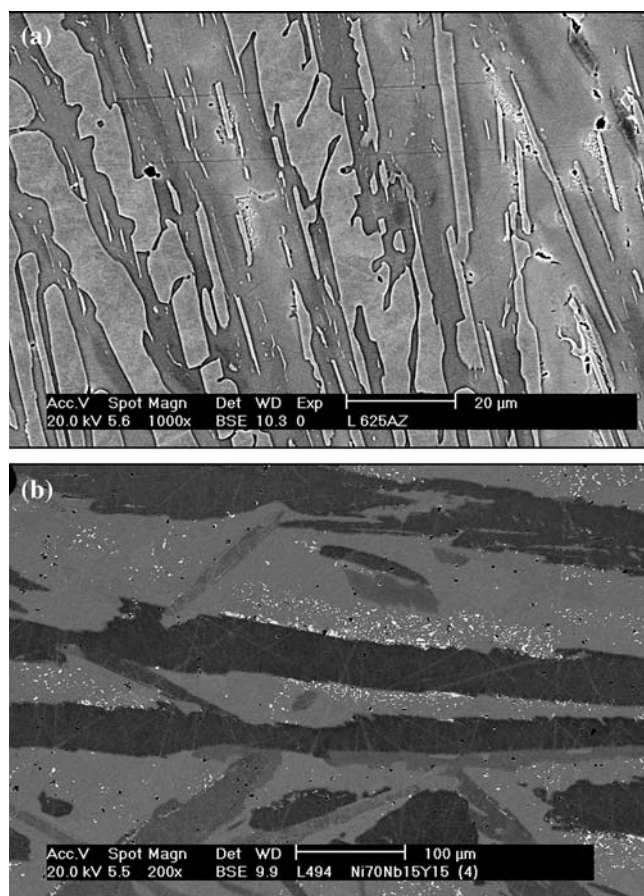
Fig. 10 SEM micrographs of the solidification microstructures of alloys in the region of the primary crystallization of $NbNi_3$. (a) Alloy 9 ($Ni_{75}Nb_{12.5}Y_{12.5}$): light elongated grains, $NbNi_3$; gray matrix, Ni_3Y; dark, Ni_7Y_2. (b) Alloy 11 ($Ni_{71.77}Nb_{13.2}Y_{15.03}$): large and dark areas, primary $NbNi_3$; middle gray shells around primary $NbNi_3$, Ni_3Y; gray matrix, Ni_2Y; small elongated grains within this matrix, secondary $NbNi_3$; white particles, μ

qualitative information was used together with the temperatures of invariant reactions determined by DSC (Table 5) and the data on liquid miscibility gap (Table 4) to optimize the composition-dependent ternary interaction parameter of the liquid phase. The experimental temperatures of four-phase equilibria are well reproduced by the calculation. The absence of systematic errors is evident from the measured temperatures of degenerated invariant reactions D_1, D_2, and D_3, which coincide with the corresponding temperatures in the binary Ni-Y system (Fig. 2) within ±10 °C. The calculated projection of liquidus surface is shown in Fig. 7. The largest area in this projection is occupied by the miscibility gap, which originates from the Nb-Y binary system and penetrates up to almost 60 at.% Ni. The solidification behavior in the ternary Nb-Ni-Y system is dominated by (Nb), μ, $NbNi_3$, and Ni_5Y phases and governed by one monotectic, two eutectic, and seven transitional invariant reactions. In addition, two invariant three-phase equilibria (Table 5) are found by calculation. The existence of these maxima is related to the congruent

melting character of the Ni_5Y and NiY phases, while their location in the projection is fully consistent with the observed solidification paths, as shown below.

The representative solidification microstructures of the alloys within the liquid immiscibility region are shown in Fig. 8. At high temperatures, alloy 23 is located in the three-phase field, where the primary (Nb) phase coexists with the two liquids, one of them vanishing at the monotectic four-phase equilibrium, $L' + L'' + (Nb) \leftrightarrow \mu$ (M_1). The remaining liquid then solidifies according to the monovariant peritectic reaction, $L'' + (Nb) \leftrightarrow \mu$, until the solidus is reached at the ternary eutectic E_2, $L'' \leftrightarrow \mu + Ni_2Y + NiY$, due to uncompleted transitional reaction U_7, $L'' + (Nb) \leftrightarrow \mu + NiY$. Note the substantial erosion of the primary (Nb) dendrites, which appear as colonies of white particles in Fig. 8(a). In alloy 19, μ is formed as a primary solid phase from the miscibility gap. Upon further decreasing temperature one of the liquids freezes completely (spherical particles in Fig. 8b), while the other still continues to precipitate the primary μ-phase of needlelike morphology. The appearance of dark shells around the needles can be understood as a result of the monovariant eutectic reaction, $L'' \leftrightarrow \mu + Ni_2Y$, while the solidification ends at the ternary eutectic E_2 (note the very fine microstructure of the gray matrix in Fig. 8b).

The field of primary crystallization of the μ-phase shows a quite large extension toward the Ni-Y edge and is partially intersected by the liquid miscibility gap (Fig. 7) at the temperature of the monotectic four-phase equilibrium. The tie-line M_1-M_1 connects the equilibrium compositions of the two liquids. The solidification microstructures of two alloys in the region of the primary crystallization of the μ-phase are shown in Fig. 9. In both alloys the monovariant eutectic reaction, $L \leftrightarrow \mu + Ni_2Y$, takes place; however, in alloy 14 it is preceded by the monovariant reaction, $L \leftrightarrow \mu + NbNi_3$, because of the higher Nb content. Because of this difference in composition, the solidification of alloy 14 stops after passing the transitional four-phase equilibrium U_6, $L + NbNi_3 \leftrightarrow \mu + Ni_2Y$, while the solidus of alloy 16 corresponds to the ternary eutectic reaction E_2.

The solidification of alloys 9 and 11 begins with the precipitation of the primary $NbNi_3$ crystals (Fig. 10). In alloy 9 it is directly followed by the monovariant peritectic reaction, $L + NbNi_3 \leftrightarrow Ni_7Y_2$; the remaining liquid freezes completely at the transitional four-phase equilibrium U_4, $L + Ni_7Y_2 \leftrightarrow NbNi_3 + Ni_3Y$. Interestingly, two different morphologies of the $NbNi_3$ phase are observed in alloy 11 (Fig. 10b) as a consequence of passing through two invariant transitional reactions: U_5, $L + Ni_3Y \leftrightarrow NbNi_3 + Ni_2Y$, and U_6, $L + NbNi_3 \leftrightarrow \mu + Ni_2Y$. After the primary $NbNi_3$ crystals are formed, the binary monovariant peritectic eutectic crystallization of Ni_3Y takes place; that is, $L \leftrightarrow NbNi_3 + Ni_3Y$. This phase is then partially consumed at the four-phase equilibrium U_5, $L \leftrightarrow Ni_3Y + Ni_2Y$, which results in appearance of the secondary $NbNi_3$ within the Ni_2Y matrix. The final stage of solidification of this alloy corresponds to the invariant reaction U_6, thus forming very fine μ-precipitates. It remains to note that in alloy 9, the monovariant reaction involving the phases L, $NbNi_3$, and Ni_7Y_2 should be preceded by another one involving the
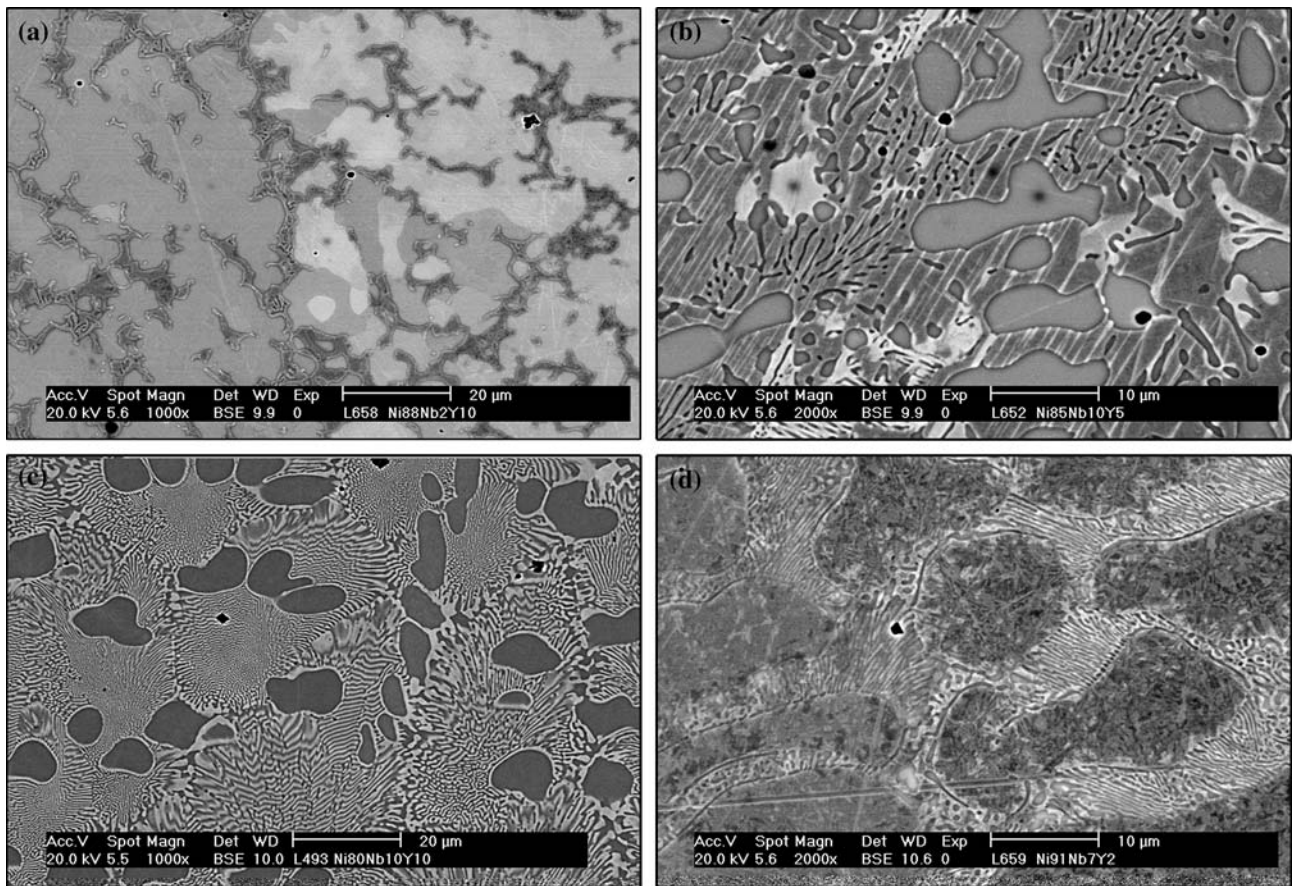
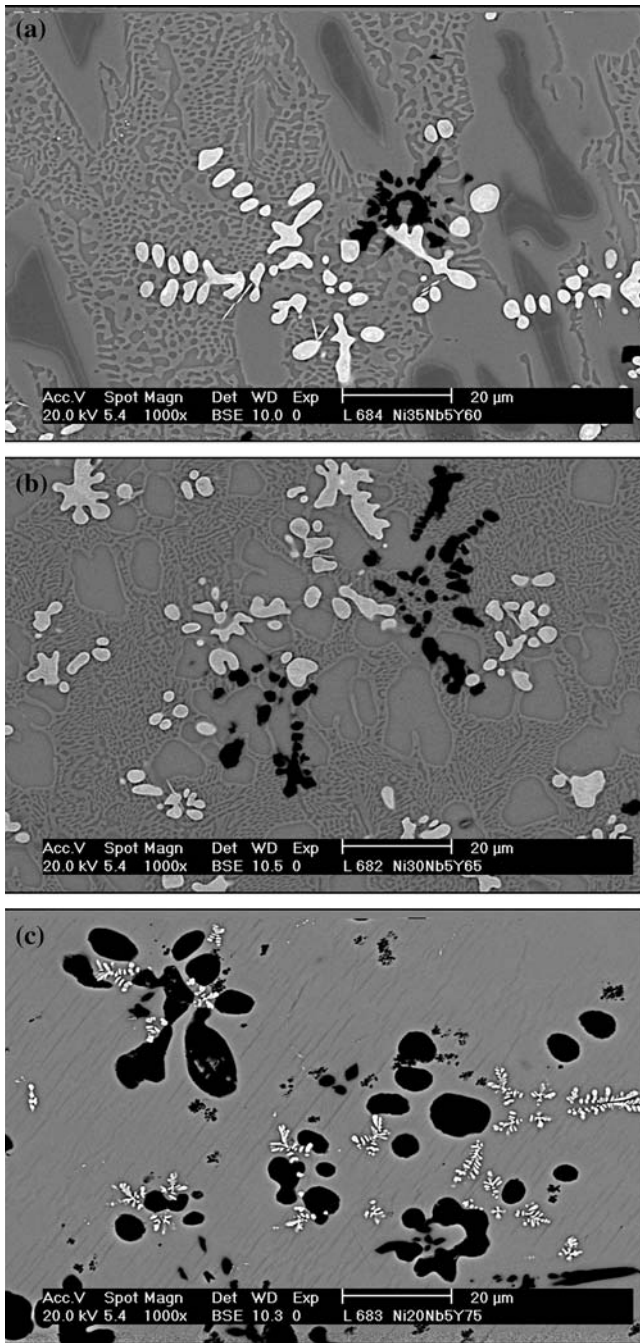**Fig. 11** SEM micrographs of the solidification microstructures of Ni-rich alloys. (a) Alloy 2 ($Ni_{88.35}Nb_{2.04}Y_{9.61}$): gray, Ni_5Y; light, $Ni_5Y + Ni_{17}Y_2$; dark patterned areas, $Ni_5Y + (Ni)$. (b) Alloy 3 ($Ni_{85.16}Nb_{9.92}Y_{4.92}$): gray, Ni_5Y; patterned matrix, $Ni_5Y + (Ni) + NbNi_3$; white inclusions, $NbNi_3$. (c) Alloy 5 ($Ni_{80.38}Nb_{9.99}Y_{9.63}$): dark grains, Ni_5Y; patterned areas (coarse), $Ni_5Y + NbNi_3$; patterned areas (fine), $Ni_5Y + (Ni) + NbNi_3$. (d) Alloy 1 ($Ni_{91.00}Nb_{7.03}Y_{1.97}$): gray, (Ni); light patterned areas, $Ni + Ni_{17}Y_2$

phases L, $NbNi_3$, and Ni_4Y. However, the amount of Ni_4Y formed after primary precipitation of $NbNi_3$ is probably so small that this phase is totally consumed through the invariant reaction U_3.

The solidification microstructures of Ni-rich alloys are shown in Fig. 11. Alloys 2, 3, 4, and 5 show the primary crystallization of Ni_5Y. Depending on composition three different solidification paths are recognized. The Nb-poor alloy 2 (Fig. 11a) exhibits the monovariant peritectic formation of the $Ni_{17}Y_2$ phase according to the reaction, $L + Ni_5Y \leftrightarrow Ni_{17}Y_2$ and freezes completely at the monovariant eutectic $L \leftrightarrow (Ni) + Ni_5Y$ (U_1-E_1). The former contains 7.3 at.% Nb as determined by EDX analysis. The microstructure of alloys 3 and 4 (Fig. 11b) shows the signs of monovariant eutectic reaction, $L \leftrightarrow NbNi_3 + Ni_5Y$, while the solidification stops at the ternary eutectic E_1, $L \leftrightarrow Ni_5Y + (Ni) + NbNi_3$. A pseudobinary eutectic microstructure corresponding to e_1 is seen very clearly in alloy 5 (Fig. 11c). The eutectic composition is measured by EDX as $Ni_{80.6}Nb_{12.0}Y_{7.4}$ (at.%), and similar values are obtained from thermodynamic calculations (Table 5). The primary crystals in alloy 1 consist of (Ni) solid solution, which contains 8.3 at.% Nb (Fig. 11d). The solidification contin-

ues via the monovariant reaction, $L \leftrightarrow (Ni) + Ni_{17}Y_2$ and should stop at the transitional four-phase equilibrium U_1. However, the Ni_5Y phase cannot be detected in the microstructure because of its low amount.

Figure 12 shows the solidification microstructures of alloys 29, 30, and 31, all containing 5 at.% Nb. After primary crystallization of (Nb), which is seen in all the alloys as white dendrites, the solidification paths depend on composition. In alloy 29, first the monovariant eutectic reaction, $L \leftrightarrow (Nb) + NiY$ takes place and then, after passing the four-phase equilibrium D_3, $L + (Nb) + NiY \leftrightarrow Ni_2Y_3$, the solidification continues via the growth of the Ni_2Y_3 phase followed by the monovariant reaction, $L + Ni_2Y_3 \leftrightarrow NiY_3$, and ends at another invariant equilibrium D_2, $L + (Nb) \leftrightarrow Ni_2Y_3 + NiY_3$. The microstructure of alloy 30 (Fig. 12b) suggests the secondary crystallization of the NiY_3 phase through the monovariant eutectic reaction, $L \leftrightarrow (Nb) + NiY_3$, which is finished at the four-phase equilibrium D_2. In alloy 31, the monovariant peritectic reaction, $L + (Nb) \leftrightarrow (Y)$ occurs (Fig. 12c), while the solidus is reached at the invariant equilibrium D_1, $L + (Nb) + (Y) \leftrightarrow NiY_3$. Note that the area marked with (Nb) in Fig. 7 comes very close to the Ni-Y boundary, so

Fig. 12 SEM micrographs of the solidification microstructures of alloys with 5 at.% Nb. (a) Alloy 29 ($Ni_{35}Nb_5Y_{60}$): white, (Nb); black, NiY; dark gray, Ni_2Y_3; light gray, NiY_3; patterned area, $NiY_3 + Ni_2Y_3$. (b) Alloy 30 ($Ni_{30}Nb_5Y_{65}$): white, (Nb); gray rounded particles, NiY_3; patterned area, $NiY_3 + Ni_2Y_3$; black dendrites (Y), nonequilibrium inclusions from arc melting. (c) Alloy 31($Ni_{20}Nb_5Y_{75}$): white, (Nb); black, (Y); gray matrix, NiY_3

that the four-phase equilibria D_1, D_2, and D_3 degenerate; that is, the liquid contains very little Nb, and thus the temperatures are not significantly different from the corresponding temperatures of three-phase equilibria in the binary Ni-Y system.
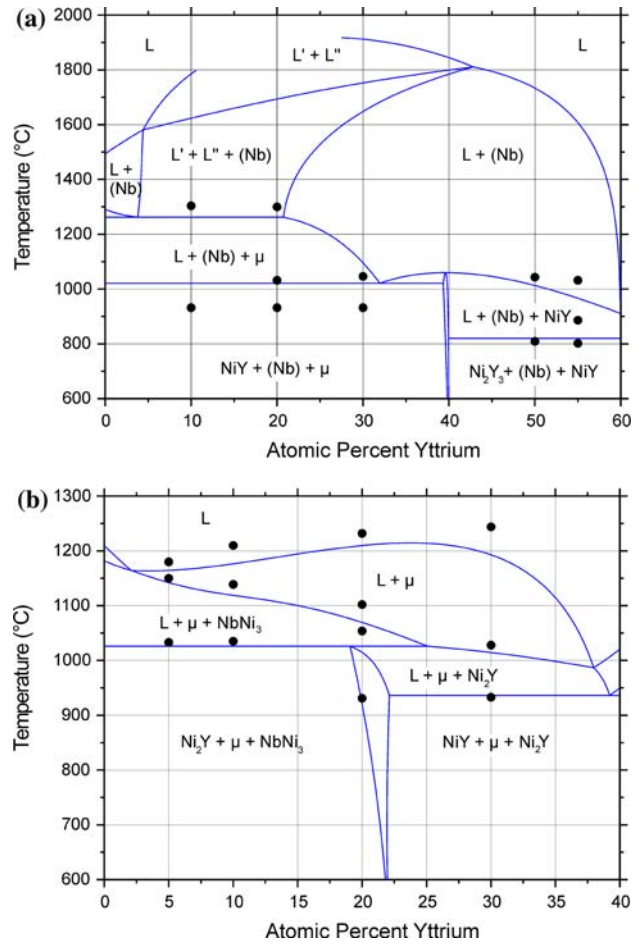
Fig. 13 Calculated temperature-composition sections of the Nb-Ni-Y phase diagram at 40 at.% Ni (a) and 60 at.% Ni (b) superimposed with experimental DSC data of this work

5.4 Temperature-Composition Sections

The calculated temperature-composition sections of the Nb-Ni-Y phase diagram are shown in Fig. 13 to 15, where solid circles correspond to the transitions from one phase field to another at the particular compositions. These temperatures are determined by the analysis of DSC heating curves as proposed by Gödecke.[18] It should be noted that because of the finite heating rate as well as the possible shifts in compositions and partial equilibration of alloys with high niobium contents, these temperatures may not be identical with those that would be measured in equilibrium conditions. Therefore, only temperatures of invariant equilibria, which appear in the sections as horizontal lines, are used in the thermodynamic optimization. The corresponding heat effects on DSC curves are always clearly detected as sharp peaks and practically not influenced by the factors mentioned previously. Even so, the lines in Fig. 13 to 15 fit all the experimental data reasonably well. Invariant reaction M_1 is detected in alloys 18, 21, and 23, U_1 in alloy 2, E_1 in alloy 4, U_2 in alloys 5 and 6, U_3 in alloy 7, U_4 in alloy 8, U_5
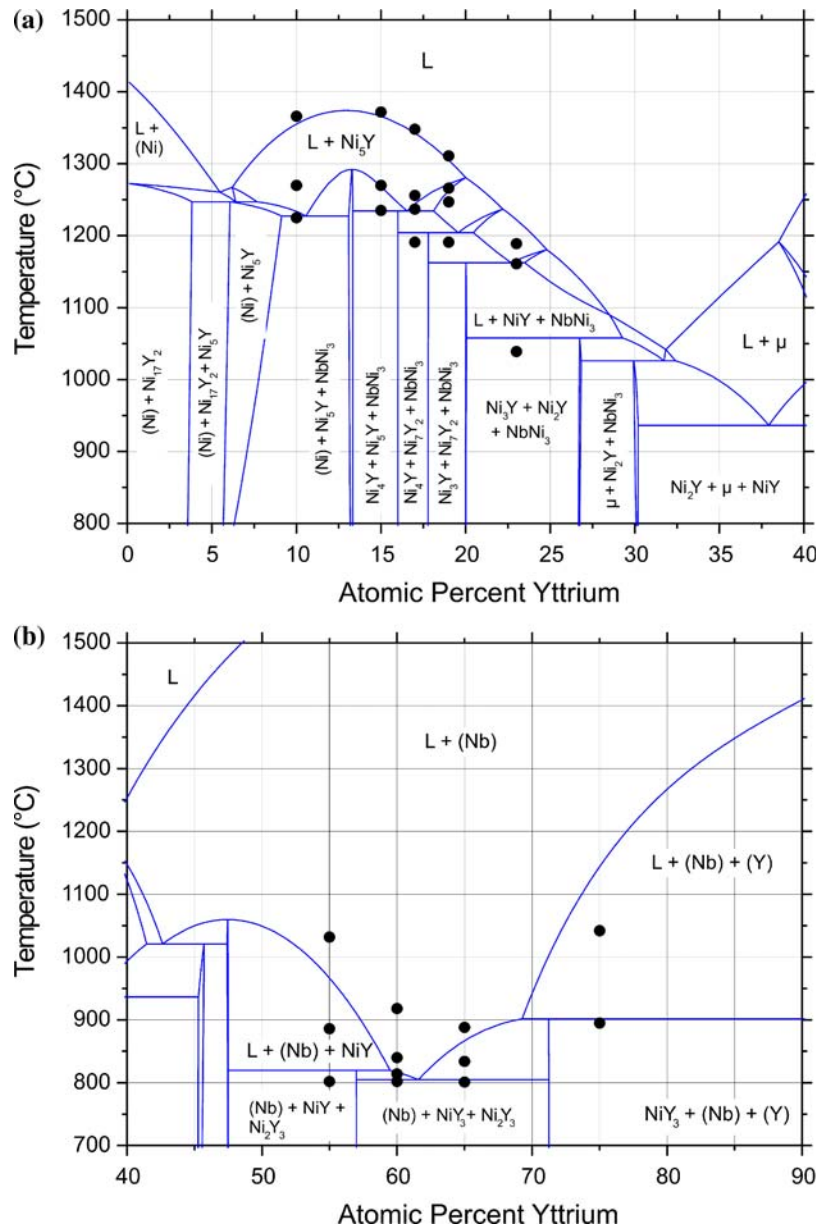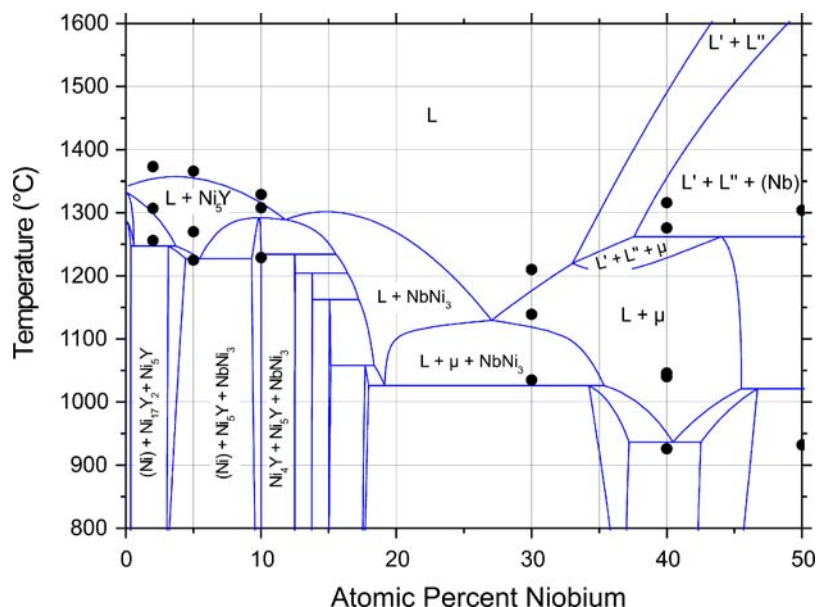
Fig. 14 Calculated temperature-composition section of the Nb-Ni-Y phase diagram at 5 at.% Nb superimposed with experimental DSC data of this work. (a) Ni-rich part. (b) Y-rich part

in alloy 10, U_6 in alloys 13 and 14, U_7 in alloys 23, and 24, E_2 in alloys 16, 18, 21, 23, 24, D_1 in alloy 31, D_2 in alloys 27, 28, 29, and 30, and D_3 in alloy 29.

Figure 13 shows two sections with the constant nickel content. At 40 at.% Ni (Fig. 13a), the liquid miscibility gap extends from 4.4 to 42.8 at.% Y, whereas at 60 at.% Ni (Fig. 13b) the liquid is homogeneous, in full agreement with experimental observations. The critical temperature of the miscibility gap at 40 at.% Ni cannot be precisely calculated, the estimated value being 1922 °C. The "ghost" thermal effects in alloys 21, 23, and 24 (Fig. 13a) correspond to the ternary eutectic E_2, because at practical cooling rates the

solidification path usually deviates from the equilibrium ones. Figure 14 shows the 5 at.% Nb section, which looks rather similar to the Ni-Y binary phase diagram, while the µ-phase and (Nb) appear only at high Y contents. This observation is consistent with the immiscibility of Nb-Y alloys and the degenerate character of four-phase equilibria near the monovariant eutectic, $L \leftrightarrow Ni_2Y_3 + NiY_3$. From Fig. 15 (section at 10 at.% Y) it is evident that ternary interactions in the Nb-Ni-Y liquid have the strongest influence on its thermodynamic properties in the region around 27 at.% Nb, while the liquid miscibility gap extends up to 33 at.% Nb.

Fig. 15 Calculated temperature-composition section of the Nb-Ni-Y phase diagram at 10 at.% Y superimposed with experimental DSC data of this work

6. Summary

Phase equilibria in the ternary Nb-Ni-Y system have been experimentally determined for the first time. Solidification microstructures have been analyzed using SEM and EDX, while thermal effects on heating and cooling have been detected by DSC. An isothermal section at 750 °C, a projection of liquidus surface, and various temperature-composition sections have been constructed with the help of thermodynamic calculations by means of the CALPHAD method. The binary Nb-Ni and Ni-Y systems have been accepted from the literature, while the thermodynamic description of the Nb-Y system has been obtained in the present work. The liquid phase as well as the terminal solid-solution phases, bcc, fcc, and cph have been described using a substitutional solution model and Muggianu interpolation of binary excess Gibbs energy. A composition-dependent ternary interaction parameter has been optimized for the liquid phase. The Nb-Ni-Y system is characterized by the wide range of liquid immiscibility (up to 60 at.% Ni), which originates from the Nb-Y binary system. One monotectic, two eutectic, seven transitional, and three degenerated four-phase invariant equilibria exist in the system.

References

1. E.S. Park and D.H. Kim, Phase Separation and Enhancement of Plasticity in Cu-Zr-Al-Y Bulk Metallic Glasses, *Acta Mater.*, 2006, **54**, p 2597
2. A.A. Kündig, M. Ohnuma, D.H. Ping, T. Ohkubo, and K. Hono, In situ Formed Two-Phase Metallic Glass with Surface Fractal Microstructure, *Acta Mater.*, 2004, **52**, p 2441
3. B.J. Park, H.J. Chang, D.H. Kim, and W.T. Kim, In situ Formation of Two Amorphous Phases by Liquid Phase Separation in Y-Ti-Al-Co Alloy, *Appl. Phys. Lett.*, 2004, **85**, p 6353
4. N. Mattern, U. Kuehn, A. Gebert, T. Gemming, M. Zinkevich, H. Wendrock, and L. Schultz, Microstructure and Thermal Behavior of Two-Phase Amorphous Ni-Nb-Y Alloy, *Scr. Mater.*, 2005, **53**, p 271
5. N. Saunders and A.P. Miodownik, *CALPHAD Calculation of Phase Diagrams*, Pergamon Materials Series, 1998
6. SGTE Unary Database version 4.4, www.sgte.org
7. M. Hillert, The Compound Energy Formalism, *J. Alloys Compd.*, 2001, **320**, p 161
8. J.-M. Joubert, B. Sundman, and N. Dupin, Assessment of the Niobium-Nickel System, *Calphad*, 2004, **28**, p 299
9. M. Hillert and M. Jarl, Model for Alloying Effects in Ferromagnetic Metals, *Calphad*, 1978, **2**, p 227
10. J.O. Andersson, T. Helander, L. Höglund, P. Shi, and B. Sundman, Thermo-Calc & DICTRA, Computational Tools for Materials Science, *Calphad*, 2002, **26**, p 273
11. PANDAT—A Multi-component Phase Diagram Calculation Software, Computherm LLC, www.computherm.com
12. A. Bolcavage and U.R. Kattner, A Reassessment of the Calculated Ni-Nb Phase Diagram, *J. Phase Equilib.*, 1996, **17**, p 92
13. H. Chen and Y. Du, Refinement of the Thermodynamic Modeling of the Nb-Ni System, *Calphad*, 2006, **30**, p 308
14. Z. Du and W. Zhang, Thermodynamic Assessment of the Ni-Y System, *J. Alloys Compd.*, 1996, **245**(1), p 164

15. Z. Du and D. Lu, Thermodynamic Modeling of the Co-Ni-Y System, *Intermetallics*, 2005, **13**, p 586

16. A. Palenzona and S. Cirafici, The Nb-Y (Niobium-Yttrium) System, *J. Phase Equilib.*, 1991, **12**, p 204

17. Y.M. Muggianu, M. Gambino, and J.P. Bros, Enthalpies of Formation of Liquid Alloys Bismuth-Gallium-Tin at 723 K—Choice of an Analytical Representation of Integral and Partial Thermodynamic Functions of Mixing for This Ternary-System, *J. Chim. Phys.*, 1975, **72**, p 83

18. T. Gödecke, Ableitung des Kristallisationspfades in ternären Gusslegierungen, *Z. Metallkd.*, 2001, **92**, p 966, (in German)